Materials Advances

ROYAL SOCIETY OF CHEMISTRY

PAPER

View Article Online
View Journal | View Issue

Cite this: *Mater. Adv.*, 2024, 5, 593

Chemically amplified molecular resins for shrinkage-controlled direct nanoimprint lithography of functional oxides: an application towards dark-light dual-mode antibacterial surfaces†

Ravikiran Nagarjuna,[a] Anindita Thakur,[b] Aniket Balapure,[a] Mohammad S. M. Saifullah,[c] Jayati Ray Dutta *[b] and Ramakrishnan Ganesan *[a]

Received 5th September 2023,
Accepted 30th November 2023

DOI: 10.1039/d3ma00666b

rsc.li/materials-advances

Although the olefin-based polymerizable sol–gel (PSG) approach has brought about significant advancements in the domain of direct and scalable nanoimprinting of oxides, the high feature size shrinkage (>75–80%) due to low metal content remains a challenge. To address this, our study introduces tailor-made bifunctional monomers containing acetoacetyl and epoxy/oxetane moieties, enabling the formulation of imprintable single-source molecular precursor-based resins with tunable metal content. The introduction of epoxy/oxetane functionality serves a multi-purpose, enabling ring-opening polymerization in a chemically amplified manner while offering additional advantages such as oxygen insensitivity, good adhesion and higher metal content by alleviating the requirement of reactive diluents. The proof-of-concept imprinting studies using resins of candidate metals (Ti, Zr and Nb) have shown a reduced feature size shrinkage of the oxides to as low as ~50%. The functionality of patterned metal oxide nanostructures is exemplified by TiO_2/AgBr nanocomposites—fabricated *via* two different approaches—displaying high antibacterial efficacy against *Escherichia coli* under dark-light dual-mode conditions. Our study opens up new avenues in the realms of direct nanoimprinting of functional inorganic materials and their biological applications.

1. Introduction

The nanostructuring of functional materials has garnered colossal significance across various domains encompassing semiconductor, magnetic, optical, biosensor and memory devices.[1,2] In the past two decades, advancements beyond conventional photolithography and electron-beam lithography have introduced a plethora of fabrication techniques that include dip-pen, nanoimprinting, electro-hydrodynamic, block co-polymer, colloidal, extreme UV and interference lithography.[3–11] Among the array of fabrication techniques, nanoimprint lithography has garnered substantial attention due to its distinct advantages such as simplicity, high fidelity, non-dependency on the optical diffraction limit, high-throughput fabrication through step-and-flash or roll-to-roll/flat and ability to imprint arbitrary structures, even over curved surfaces.[12–18]

While polymeric materials have predominantly been used in these techniques, there has been a recent surge in the direct fabrication of functional inorganic nanomaterials.[19–25] In particular, direct nanoimprinting of metal oxides has emerged as an attractive avenue owing to their wide-ranging applications.[13,26–29] Notably, a unique characteristic of metal oxide nanoimprinting is the shrinkage of feature size in the final patterned structures, primarily influenced by the total metal content in the resin or ink.[30,31] While this feature size reduction can be advantageously employed to achieve nanoscale features using molds containing sub-micron patterns, the tunability of the metal content becomes a crucial criterion in determining the overall ceramic content, which subsequently governs the resulting pattern density. Recent developments in

[a] *Department of Chemistry, Birla Institute of Technology and Science (BITS), Pilani, Hyderabad Campus, Jawahar Nagar, Kapra Mandal, Medchal District, Hyderabad, Telangana – 500 078, India. E-mail: ram.ganesan@hyderabad.bits-pilani.ac.in*
[b] *Department of Biological Sciences, Birla Institute of Technology and Science (BITS), Pilani, Hyderabad Campus, Jawahar Nagar, Kapra Mandal, Medchal District, Hyderabad, Telangana – 500 078, India. E-mail: jayati@hyderabad.bits-pilani.ac.in*
[c] *Laboratory for Micro and Nanotechnology, Paul Scherrer Institut, Forschungsstrasse 111, 5232 Villigen PSI, Switzerland*

† Electronic supplementary information (ESI) available. See DOI: https://doi.org/10.1039/d3ma00666b

utilizing nanoparticle suspensions in direct nanoimprinting of oxides have shown significant promise in alleviating the limitations associated with the conventional sol–gel approach, such as low yield and poor mechanical strength. Although this method has been augmented successfully for fabricating three-dimensional structures of functional oxides[32] with a significant minimization of the pattern size shrinkage, the reliance of the resin on a solvent-permeable poly(dimethylsiloxane) (PDMS) mold may limit its potential in high throughput fabrication. In contrast, the polymerizable sol–gel approach (PSG), which utilizes a polymerizable liquid precursor, has been shown to be promising in high throughput techniques like step-and-flash imprint lithography.[12,30,33] Though the initial works in this approach employed moisture-sensitive resins obtained by reacting metal alkoxides with polymerizable carboxylate derivatives like methacrylic acid or vinyl acetic acid, later works overcame this moisture-sensitiveness and enhanced the shelf-life of the methacrylate precursors by employing acetylacetone-based chelating monomers.[31,34,35] Nevertheless, the methacrylate-based monomers require the purging of inert gas to keep off the dissolved oxygen, which otherwise scavenges the free radicals and thereby impacts the degree of polymerization. This constraint was overcome by employing thiol–ene click chemistry, which is known to be oxygen insensitive.[36] Despite all these advancements, the lower metal content in the imprintable resin remains a challenge, leading to significant pattern size shrinkage to the tune of 70–80%.

The current work focuses on judicious control over the metal content in the imprintable resin while at the same time exploring a non-alkene-based monomer. The goal is to tackle the excessive feature size shrinkage while maintaining the essential requirements for direct nanoimprinting. Two bifunctional monomers containing an acetoacetyl group at one end and a photogenerated acid-triggered ring-openable epoxy or oxetane moiety at the other end were designed and synthesized.[37] These monomers, upon chelating with the metal ions, enabled the formation of molecular precursor-based chemically amplified resins (CARs), using which the pattern size reduction has been brought down significantly when compared to the methacrylate-based PSG route. To the best of our knowledge, this is the first report on single-source metal-containing molecular precursor-based CARs for the direct nanoimprinting of metal oxides. By employing CARs comprising complexes of respective metals, here we demonstrate proof-of-concept studies on the fabrication of representative oxides like TiO_2, ZrO_2 and Nb_2O_5. It can be noted that previous reports on oxide nanoimprinting *via* the PSG approach utilized commercially procured monomers. Whereas the current work introduces custom-designed and synthesized CAR-based monomers that fulfill the essential requirements for imprintable resin. Additionally, CARs are known to exhibit oxygen insensitivity, providing the advantage of alleviating any requirement to eliminate oxygen during the imprinting process. Moreover, the inherent high adhesion property of the cyclic ethers facilitates spin-coating of the formulations, yielding high-quality films without the need for any reactive diluents, thereby offering better control over the metal content.

Shifting gears, materials and technologies that mitigate the spread of microbial pathogenesis are the need of the hour, particularly in the backdrop of antimicrobial resistance leading to the formation of multidrug-resistant strains.[38–41] Several photocatalytic materials based on oxides have been developed for bactericidal and environmental remediation purposes to mitigate antimicrobial resistance.[42,43] A biomimetic array of TiO_2 patterns with shark-skin architecture was found to have enhanced antibacterial activity under UV light irradiation.[44] Though several materials are being developed for this purpose, the majority of them are active either under dark or light conditions.[45–47] Recently, a few literature have reported photocatalytically-active materials that exhibit antibacterial activity under dark-light dual mode.[48–52] Nevertheless, such materials fall under the category of powders and hence, the development of dual mode-active coatable compositions could be highly beneficial and attractive for rendering numerous frequently touched surfaces with antibacterial properties, especially in high-risk areas like hospitals and public places.[53,54] Therefore, as a potential application of the oxide nanoimprinting route employed here, we chose the popular photocatalyst TiO_2 to further create heterojunction with AgBr.[55,56] The obtained nanostructures have been studied for their efficacy towards dark-light dual-mode disinfection characteristics.

2. Results and discussion

Typically, the imprintable metal-containing resins in the PSG approach consist of following components: a metal–monomer complex, reactive diluent(s) and a polymerization initiator.[31] The monomer usually possesses a polymerizable functional group (*e.g.*, acrylates) and a chelating moiety (*e.g.*, acetoacetate). It is essential to balance the amount of organic content in the resin to impart good film formability, for which the reactive diluents have been highly beneficial. However, the higher organic content comes with a trade-off in the final metal content, causing excessive feature size shrinkage during the calcination step to yield the corresponding metal oxide. Keeping these factors into consideration, we aimed to increase the metal content in the resin formulation to increase the overall ceramic yield and thereby decrease the shrinkage. It can also be noted that the methacrylate-based resins give rise to a shrinkage in the range of 10–40% during the polymerization stage itself,[31] which indicates the presence of a significant void space in the pre-polymer film, plausibly arising due to the molecular packing. Scheme 1 illustrates the comparison of metal content between the resin formulations used in this study with the previous reports and also presents the process flowchart of nanoimprinting using CAR-based metal-containing resins developed in this work.

In this work, we designed two low molecular weight monomers that contain an epoxy or an oxetane group at one end that could undergo cationic ring-opening polymerization and an

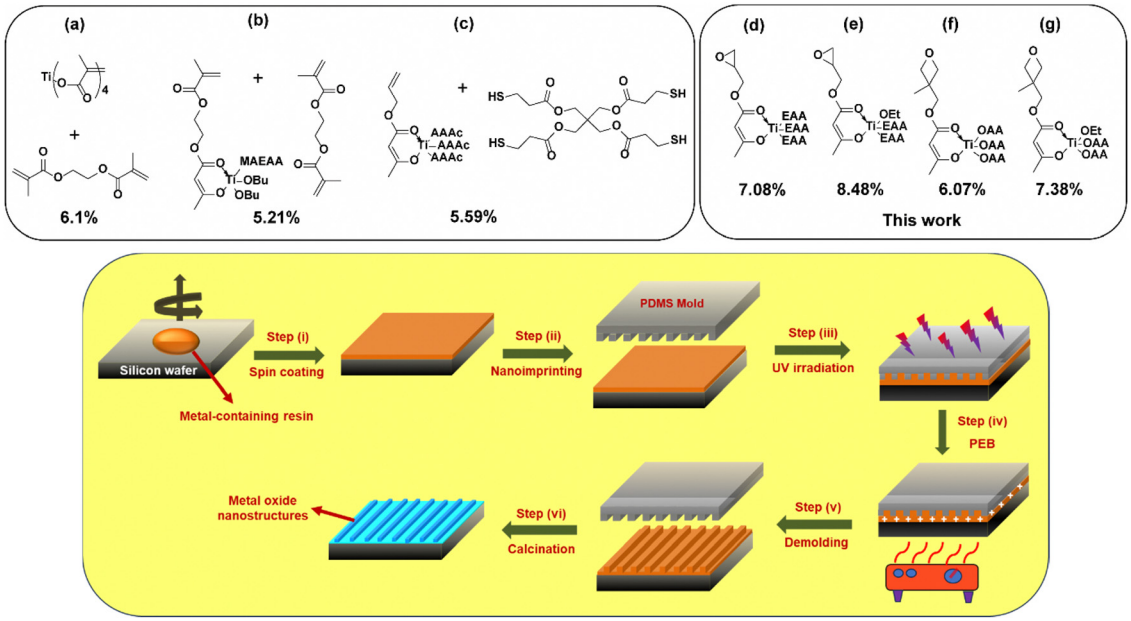

Scheme 1 Top panel: Comparison of the metal content in various titanium-containing resins employed in PSG-based nanoimprinting approaches. The molecular mass of the resins was estimated from the overall dry weight of the metal-containing monomer and crosslinker (if present), as per the molar ratio reported in the literature, from which the wt% of the metal is determined and presented alongside the formulations. For easy visualization, in most of the metal-containing monomers, one arm having reactive functionality has been depicted, while components of the other three arms have been shown by the abbreviations as mentioned in the original reference of the monomer. The abbreviations 'OEt' and 'OBu' represent 'ethoxy' and 'butoxy' moieties, respectively. The resins represented in (a), (b) and (c) are taken from the respective ref. 30, 31 and 36. Bottom panel: Schematic representation of the overall process involving ring opening polymerization chemistry for the direct nanoimprinting of metal oxides.

acetoacetate group on the other end to facilitate chelation with the metal of interest. Among the two monomers, epoxy-functionalized acetoacetate (EAA) was synthesized through a *trans*-esterification reaction between *tert*-butyl acetoacetate (*t*-BAA) and glycidol, as reported in the literature.[57] Though there is no literature report on the synthesis of oxetane-functionalized acetoacetate (OAA), the transacetoacetylation reaction between *t*-BAA and 3-methyl-3-oxetane methanol was found to be successful in yielding OAA. The synthesized monomers were structurally characterized using nuclear magnetic resonance (NMR) spectroscopy. The ^{1}H NMR spectrum of EAA in Fig. 1(a) shows the characteristic peaks at δ values of 2.28 (s, 3 H_a), 2.67 (dd, 1 H_f), 2.86 (dd, 1 H_g), 3.23 (m, 1 H_e), 3.53 (s, 2 H_b), 4.0 (dd, 1 H_c) and 4.42 (dd, 1 H_d). The peak assignments of the characteristic signals have been depicted using the chemical structure, as shown in the figure. Further, the ^{13}C NMR spectrum shows peaks with δ values of 30.12 (C_7), 44.53 (C_1), 49.06 (C_5), 49.57 (C_2), 65.59 (C_3), 166.80 (C_4), 200.27 (C_6) in Fig. S1 (ESI†). Both the spectra were found to be matching with the reported values and thus confirmed the successful synthesis of EAA.[57] Fig. 1(b) shows the ^{1}H NMR of OAA with the distinctive peaks at δ values of 1.34 (s, 3H_d), 2.28 (s, 3 H_a), 3.54 (s, 2 H_b), 4.24 (d, 2 H_e), 4.39 (d, 2H_f) and 4.52 (d, 2 H_c). The ^{13}C NMR spectrum of OAA shows the respective peaks with δ values at 21.09 (C_3), 30.18 (C_8), 39.02 (C_2), 49.84 (C_6), 69.37 (C_4), 77.46 (C_1), 167.15 (C_5) and 200.32 (C_7) (Fig. S1, ESI†). The chemical shift, splitting pattern and integral values confirm the successful synthesis of OAA. It can be noted that both the overall percentage yield of the purified product and shelf-life were found to be higher with OAA, which could be attributed to the fact that the 3-membered epoxy ring is highly strained and hence more reactive than the 4-membered oxetane ring.

To formulate the imprintable resin, the synthesized monomers, such as EAA and OAA, were treated with metal alkoxides to obtain the corresponding epoxy- and oxetane-functionalized metal complexes. Fig. S2 (ESI†) shows the plausible chemical reactions between EAA/OAA and a metal alkoxide by chosing titanium ethoxide as a model substance. The ethoxy group is reported to exhibit two ^{1}H NMR signals at 1.25 and 4.35 ppm corresponding to (C***H***$_3$) and (C***H***$_2$) protons, respectively.[58] To probe the metal–monomer chelation, titanium ethoxide was reacted with the synthesized monomers in a 1 : 4 ratio and the ^{1}H NMR spectra of the obtained products, Ti(EAA)$_4$ and Ti(OAA)$_4$, were recorded (Fig. 1). After chelation, three characteristic peaks of protons in free ethanol were observed at δ values 1.22 (m, C***H***$_3$), 3.71 (m, C***H***$_2$) and 1.98 (s, O***H***), which confirmed the successful displacement of ethoxy groups by the acetoacetate moieties in a stoichiometric manner.[58] Besides, the spectrum of Ti(EAA)$_4$ was largely found to be similar to that of EAA, except for a small peak δ = 5.05 corresponding to the proton in the enolate form of the complex (COC***H***CO), which is suggestive of the chelation through keto–enol tautomerism.[34] A similar pattern in the ^{1}H NMR was observed with Ti(OAA)$_4$ as well. It is worth noting that the characteristic peaks of epoxy and oxetane groups remained intact during the reaction and thus were found to be stable.

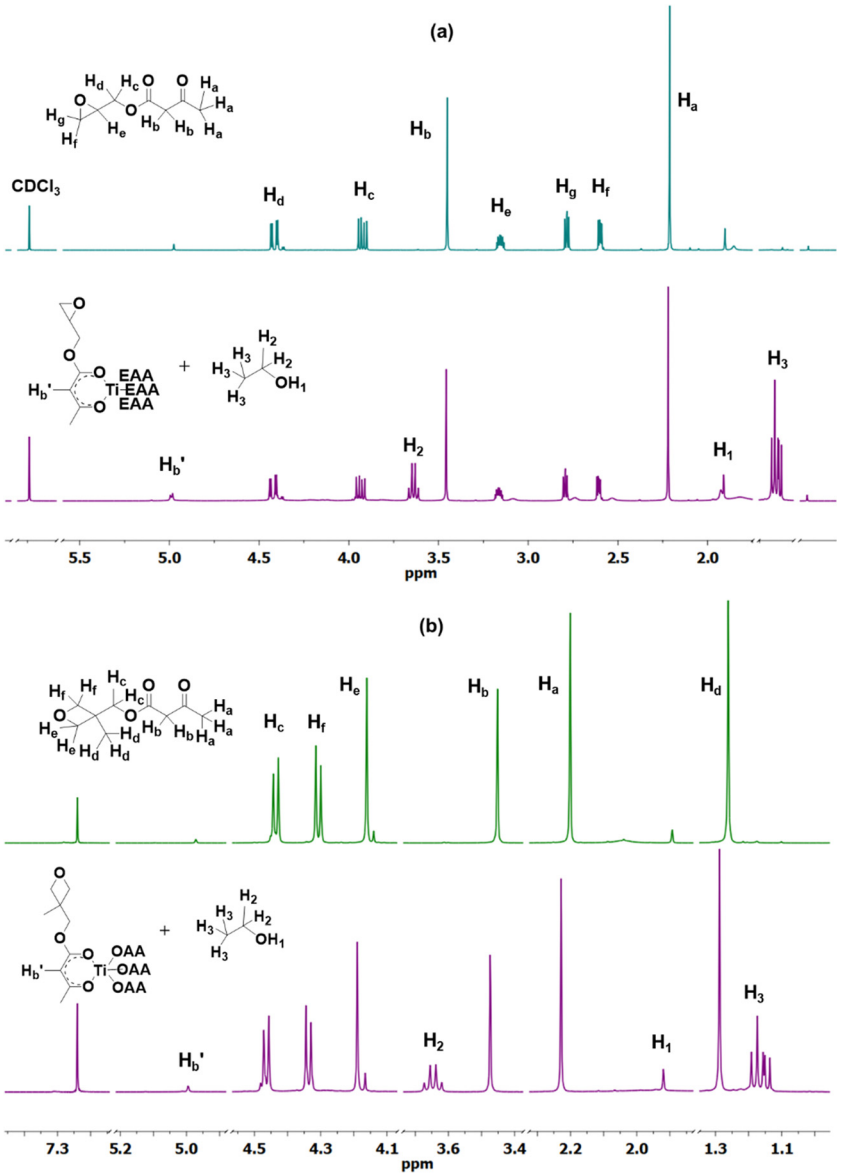

Fig. 1 ^{1}H NMR spectra of EAA (a) and OAA (b) before and after complexation with titanium(IV) ethoxide to formulate $Ti(EAA)_4$ and $Ti(OAA)_4$ resins. The respective chemical structures shown in the inset are labelled for indicating the characteristic peaks.

To further validate the chelation of the acetoacetate group of the monomers with the metal and also explore the ring-opening polymerization, Fourier transform infrared (FT-IR) spectroscopic studies of $Ti(EAA)_4$ and $Ti(OAA)_4$ were performed. It was observed from Fig. 2(a) that EAA showed prominent characteristics peaks at 1746 cm^{-1} and 1712 cm^{-1} corresponding to the ester and keto carbonyl groups, respectively, besides a characteristic epoxy signature peak at 911 cm^{-1}.[59,60] While the FT-IR spectrum of $Ti(EAA)_4$ resin largely resembled that of as-synthesized EAA, two new peaks were also observed at 1624 cm^{-1} and 1532 cm^{-1}, which could be attributed to the chelation of the carbonyl group in the enol form of EAA with the metal center. The two peaks observed represent the asymmetric and symmetric stretching vibrations of the carbonyl group in the chelated keto–enol form, which binds to the metal center in a bidentate manner.[31] After UV exposure and a subsequent post-exposure bake (PEB) step to induce crosslinking, the spectrum of the resin remained almost similar to that of the as-prepared one, except for the epoxy peak. The signature epoxy functional group peak at 911 cm^{-1} was found to completely disappear after PEB, indicating the participation of the epoxy functional group in the ring-opening polymerization reaction. The intensity of peaks corresponding to the chelation was found to remain unchanged even after the polymerization, indicating the stability of the metal–monomer chelation. A similar trend was also observed with the Ti-containing OAA resin (Fig. 2(b)). In this case, the characteristic oxetane ring breathing peak at 979 cm^{-1} was found to disappear after curing, which confirmed the occurrence of cationic ring-opening polymerization in this system as well.[61]

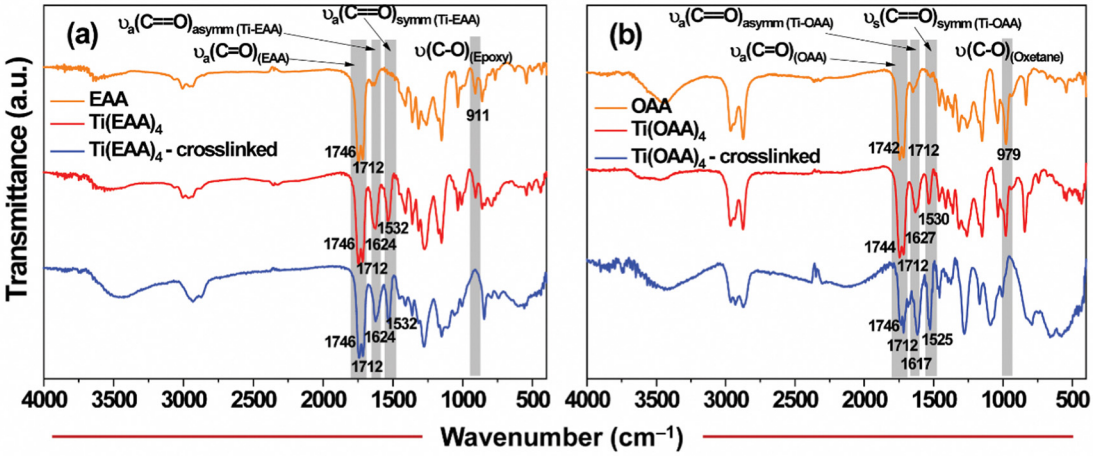

Fig. 2 Probing of metal chelation and ring opening polymerization in (a) $Ti(EAA)_4$ and (b) $Ti(OAA)_4$ resin formulations through FT-IR analyses.

As mentioned earlier, the study aims to minimize the organic content while fulfilling other requirements such as good film formability, fluidity to fill into the mold cavities, polymerizability for resin solidification during imprinting and adequate mechanical strength to withstand demolding pressures. Comparing the molar mass of ethoxide and EAA, the latter is 3.5 times heavier than the former. Consequently, to verify the lowest possible organic content in an imprintable resin, we formulated compositions such as $Ti(OEt)_3$(EAA/OAA), $Ti(OEt)_2$(EAA/OAA)$_2$, $Ti(OEt)$(EAA/OAA)$_3$ and Ti(EAA/OAA)$_4$ by progressively increasing the stoichiometry of EAA/OAA in place of each ethoxide arm in $Ti(OEt)_4$. The thermogravimetric analyses (TGA) of all such resin formulations—incorporated with 2 wt% of photoacid generator (PAG) and subjected to UV irradiation—were performed under air atmosphere to probe the thermal degradation profile and the residual metal oxide content (Fig. 3). It can be seen from the figure that the first step of mass loss occurred between 100 and 350 °C, corresponding to the weakly-bound monomers and/or low molecular weight oligomers. The second step of mass loss between 350 and 550 °C could be attributed to the thermal decomposition of the crosslinked polymer. Above 550 °C, a stable plateau at a certain residual mass was observed, which confirmed the formation of the metal oxide. As expected, the mass loss was increased as the content of the monomer in the resin formulation was increased. For instance, The residual mass of TiO_2 from $Ti(EAA)_4$ was 11.5% as opposed to 29.4% from $Ti(OEt)_3$(EAA). A similar trend was observed with OAA-based formulations as well. Table 1 summarizes the comparison between the estimated residual metal oxide content in various formulations with the values obtained from the TGA measurements, which revealed a reasonable match between the two. The slightly higher experimental values observed in some compositions may be attributed to the potential evaporation of a small amount of the monomer/alkoxy moiety during UV irradiation and sample loading for TGA measurements.

As mentioned in Table 1, four resist formulations using each monomer along with 2 wt% of PAG were prepared and studied for their imprintability. The morphology of the imprints before and after calcination was analyzed using field-emission scanning electron microscopy (FE-SEM). The PDMS mold used for the imprinting had the line and space pattern widths as ~2.15 μm and ~1.75 μm, respectively. After ring-opening polymerization, the thin films obtained with $Ti(OEt)_3$(EAA) and $Ti(OEt)_3$(OAA) were found to be brittle and peeled off on demolding and hence were found not suitable for imprinting

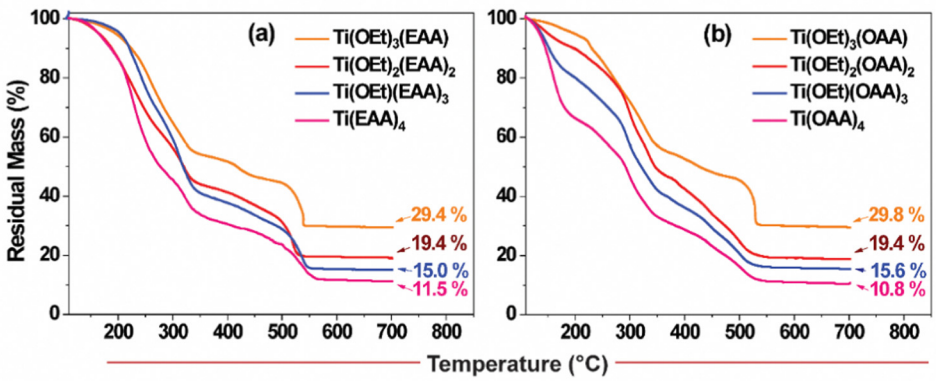

Fig. 3 TGA profiles of the resin formulations having different ratios of titanium(IV) ethoxide to EAA/OAA: (a) EAA-based and (b) OAA-based resins.

Table 1 Calculated and experimental residual mass of TiO_2 in different resin formulations presented in Fig. 3

	Residual mass of TiO_2 (%)	
Sample code	Calculated	Experimental
$Ti(OEt)_3(EAA)$	23.5	29.4
$Ti(OEt)_2(EAA)_2$	17.6	19.4
$Ti(OEt)(EAA)_3$	14.1	15.0
$Ti(EAA)_4$	11.8	11.5
$Ti(OEt)_3(OAA)$	21.7	29.8
$Ti(OEt)_2(OAA)_2$	15.7	19.4
$Ti(OEt)(OAA)_3$	11.8	15.6
$Ti(OAA)_4$	10.1	10.8

The calculated residual mass was based on the dry mass of the metal–monomer complex. The displaced ethanol and 2 wt% of PAG were not accounted.

(data not shown). This could be due to the lesser monomer content that could have resulted in a poorer degree of polymerization and, thereby, lacking the mechanical stability to sustain the pattern integrity. Though the imprintability was found to be substantially improved in $Ti(OEt)_2(EAA)_2$ and $Ti(OEt)_2(OAA)_2$, significant cracks were observed at the macroscopic scale (Fig. S5, ESI†), due to which a substantial flaking off of the films occurred during calcination. When the metal-to-monomer ratio was increased to 1 : 3 and 1 : 4, the obtained imprints were found to be smoother and mechanically stable, even after calcination. Fig. 4 shows the aerial and cross-sectional morphologies of the imprints obtained using $Ti(OEt)(EAA)_3$, $Ti(EAA)_4$, $Ti(OEt)(OAA)_3$ and $Ti(OAA)_4$. Comparing $Ti(OEt)(EAA)_3$ and $Ti(EAA)_4$, the respective widths of the as-imprinted line and space were found to be in the range of ~1.5–1.6 μm and 2.3–2.4 μm. This has shown that the cross-linking and drying off of the resin leads to ~10% of shrinkage during the imprinting step itself. After calcination, ~48% shrinkage in the pattern width was observed with $Ti(OEt)(EAA)_3$, while that with $Ti(EAA)_4$ was found to be ~60%. This higher shrinkage with $Ti(EAA)_4$ is in line with the decreasing metal content with increasing monomer content. The magnitude of pattern width shrinkage in the case of $Ti(OEt)(OAA)_3$ and $Ti(OAA)_4$ was found to be very closer to the respective EAA counterparts. The findings revealed that the most favorable formulation for achieving successful imprinting with minimal shrinkage was the compositions comprising a 1 : 3 ratio of the metal alkoxide to the monomer. Notably, the shrinkage obtained in this study was considerably lower, in contrast to the ~75% shrinkage reported in previous studies involving (meth)acrylate and thiol–ene-based direct nanoimprinting techniques.[12,31,33,35,36] Additional experiments were conducted using dimple molds with Ti-EAA based resins to produce nanopillars to investigate pattern shrinkage in a circular geometry. In this case, the employment of $Ti(OEt)(EAA)_3$ resulted in a diameter shrinkage of 30% following calcination, whereas with $Ti(EAA)_4$, a slightly higher shrinkage of 34% was observed. It is worth mentioning that the diameter shrinkage of nanopillars after calcination using the methacrylate-based Ti-containing resins was previously

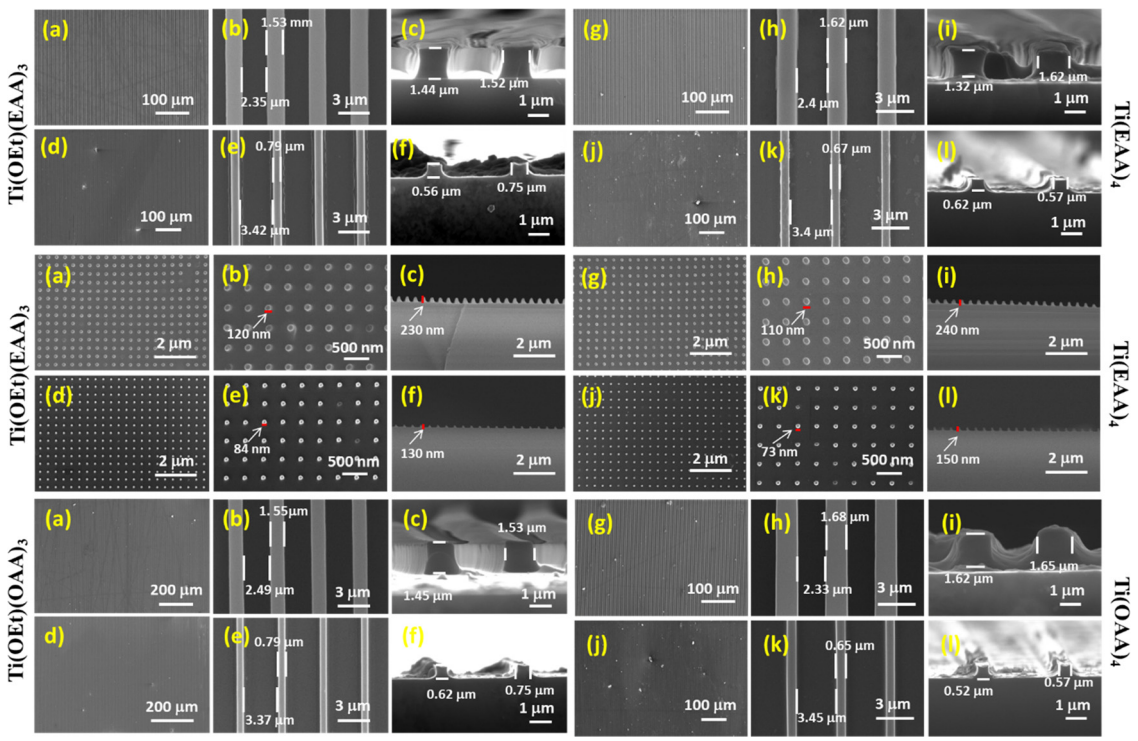

Fig. 4 Aerial and cross-sectional FE-SEM images of the imprints obtained using different resin formulations: $Ti(OEt)(EAA)_3$ (top and middle left panels: a–f), $Ti(EAA)_4$ (top and middle right panels: g–l), $Ti(OEt)(OAA)_3$ (bottom left: a–f) and $Ti(OAA)_4$ (bottom right: g–l). The top and bottom lanes in each panel represent imprints before and after calcination, respectively.

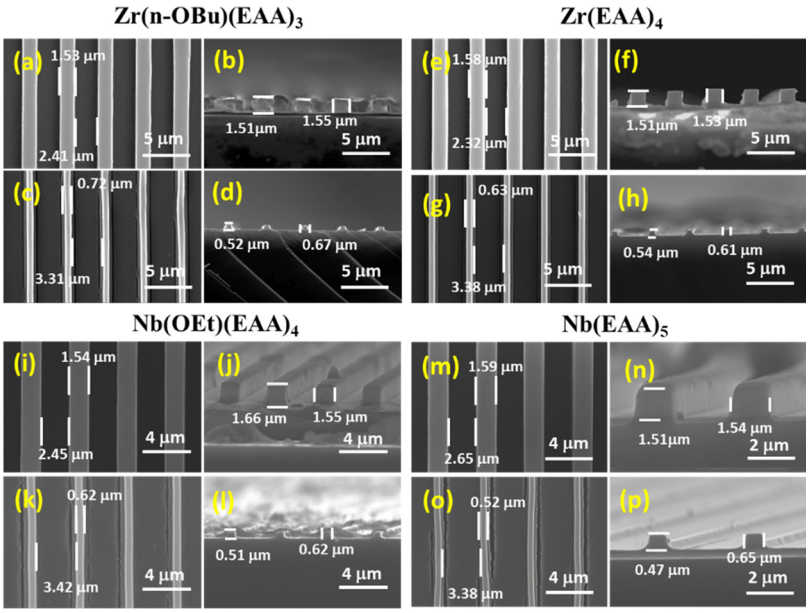

Fig. 5 Aerial and cross-sectional FE-SEM images of the imprints obtained using resin formulations of Zr(*n*-OBu)(EAA)$_3$ (a)–(d), Zr(EAA)$_4$ (e)–(h), Nb(OEt)(EAA)$_4$ (i)–(l) and Nb (EAA)$_5$ (m)–(p). The top and bottom lanes in each panel represent imprints before and after calcination, respectively.

reported to be ~50%.[33] It can further be noted that the X-ray diffraction (XRD) analyses of the calcined films obtained using Ti(EAA)$_4$ and Ti(OAA)$_4$ confirmed the formation of the anatase crystalline phase of TiO_2 (Fig. S6, ESI†).

Two additional candidates, Zr and Nb, were selected for the imprinting experiments to evaluate the versatility of the CAR-based approach utilized in this study for different metal oxides. To achieve this, Zr(*n*-OBu)$_4$ and Nb(OEt)$_5$ were reacted with appropriate amounts of EAA, resulting in the generation of Zr(*n*-OBu)(EAA)$_3$, Zr(EAA)$_4$, Nb(OEt)(EAA)$_4$ and Nb(EAA)$_5$ complexes. The FE-SEM images in Fig. 5 depict the line and space patterns of the as-imprinted resins before and after the calcination process. The results have demonstrated good imprintability of the CAR-based resins for these candidates, in which the overall pattern size shrinkage was slightly lesser than the methacrylate-based approach. In the case of niobium oxide, cracks were detected alongside the line patterns, consistent with previous findings.[33] These cracks appear to stem from excessive cross-linking and stress within the residual layer. A notable distinction in pattern distortion and cracking emerged when comparing oxides obtained using Nb(OEt)(EAA)$_4$ and Nb(EAA)$_5$ resin formulations, highlighting the influence of cross-linking intensity on the outcome. Also, the homogeneity and percentage shrinkage of the nanostructures presented in this work could be ascertained and compared with earlier-reported PSG resins using techniques like variable angle spectroscopic ellipsometer (VASE) and grazing incidence small angle X-ray scattering (GI-SAXS). Fine-tuning these parameters could potentially mitigate the observed cracking and enhance the pattern quality. Table 2 summarizes the feature size shrinkage of the line and space patterns of all the resin formulations employed in this work.

To demonstrate the functionality of the imprinted nanostructures, we chose TiO_2 as the model compound, known for its high photocatalytic activity, chemical resistance, non-toxicity and optimal valence and conduction band positions for generating reactive oxygen species (ROS).[62–65] Nevertheless, its wide band gap (3.2 eV) requires ultraviolet radiation to produce photogenerated electrons and holes. A plethora of literature is available on enhancing the photocatalytic activity of TiO_2 by creating heterojunctions with various other visible-light active semiconductors.[66–68] On a different note, thin film coatings that exhibit disinfection characteristics under dark and visible-light conditions are the urgent need of the hour, particularly in the wake of antimicrobial resistance. It can be noted that silver-based materials exhibit excellent antibacterial activities under dark conditions, while silver halides are preferred choices in heterojunction photocatalysts.[69–71] Keeping these factors in view, we conducted a proof-of-concept study focusing on nanocomposites of TiO_2 with AgBr to demonstrate the potential application of thin film metal oxide nanostructures. This combination was chosen due to AgBr's dual functionality as a photosensitizer and a dark-active antimicrobial substance.[48] Also, the combination is known to yield Type-II heterojunction, possessing favorable attributes for high photocatalytic activity.[72] Our initial approach involved mixing a surfactant-based precursor of AgBr, specifically the silver nitrate–tetraoctylammonium bromide complex (Ag–TOAB), with a Ti-containing resin to achieve a homogeneous nanocomposite. However, this addition of the AgBr precursor led to resin destabilization and subsequent precipitation. When we attempted the same procedure with the methacrylate-based Ti-containing resin reported in the literature, a similar destabilization of the resin was observed.[31] In light of these

Table 2 Summary of feature size shrinkage of various resin formulations employed in this study after imprinting as well as calcination. The mold employed for the imprinting consisted of line and space dimensions of ~2.15 μm and ~1.75 μm, respectively. The feature size shrinkage for the respective metal oxide nanostructures obtained using the methacrylate-based PSG approach reported in ref. 31 is presented alongside for comparison

Resin	Feature size of the imprint after ring opening polymerization		Metal oxide feature size after the heat-treatment of imprinted structures		Total feature size reduction with respect to mold feature size (%)	Total feature size reduction for the corresponding metal oxide as per ref. 31
	Width of imprint (μm)	Feature size reduction (%)	Width of the metal oxide feature (μm)	Feature size reduction (%)		
$Ti(OEt)(EAA)_3$	1.53	12	0.79	48	55	84
$Ti(EAA)_4$	1.62	8	0.67	59	62	84
$Ti(OEt)(OAA)_3$	1.55	11	0.79	49	55	84
$Ti(OAA)_4$	1.68	4	0.65	61	63	84
$Zr(n\text{-}OBu)(EAA)_3$	1.53	12	0.72	53	59	74
$Zr(EAA)_4$	1.58	10	0.63	60	64	74
$Nb(OEt)(EAA)_4$	1.54	12	0.62	60	65	77
$Nb(EAA)_4$	1.59	9	0.52	67	70	77

The dimensions represented here are obtained with a standard deviation of ±5%.

challenges, we employed two alternative methods to establish heterojunctions between TiO_2 and AgBr: (i) a one-step method, in which Ag–TOAB complex was spin-coated over the as-imprinted $Ti(OEt)(OAA)_3$ resin, followed by thermolysis; and (ii) a two-step method, wherein the TiO_2 nanostructures have been produced in the first step, followed by spin-coating and calcination of Ag–TOAB on top of them. The obtained nanostructures were characterized using FE-SEM, elemental mapping, X-ray photoelectron spectroscopy (XPS) and XPS valence band (VB) measurements. Due to the very thin nature of the samples, XRD measurements did not show any difference with the deposition of AgBr (data not shown).

Fig. 6(i) and (ii) show the FE-SEM images of the TiO_2/AgBr nanocomposites obtained *via* both methods. The nanocomposite obtained through the one-step method resembled the pristine TiO_2, whereas, in the two-step method, a few particulates were

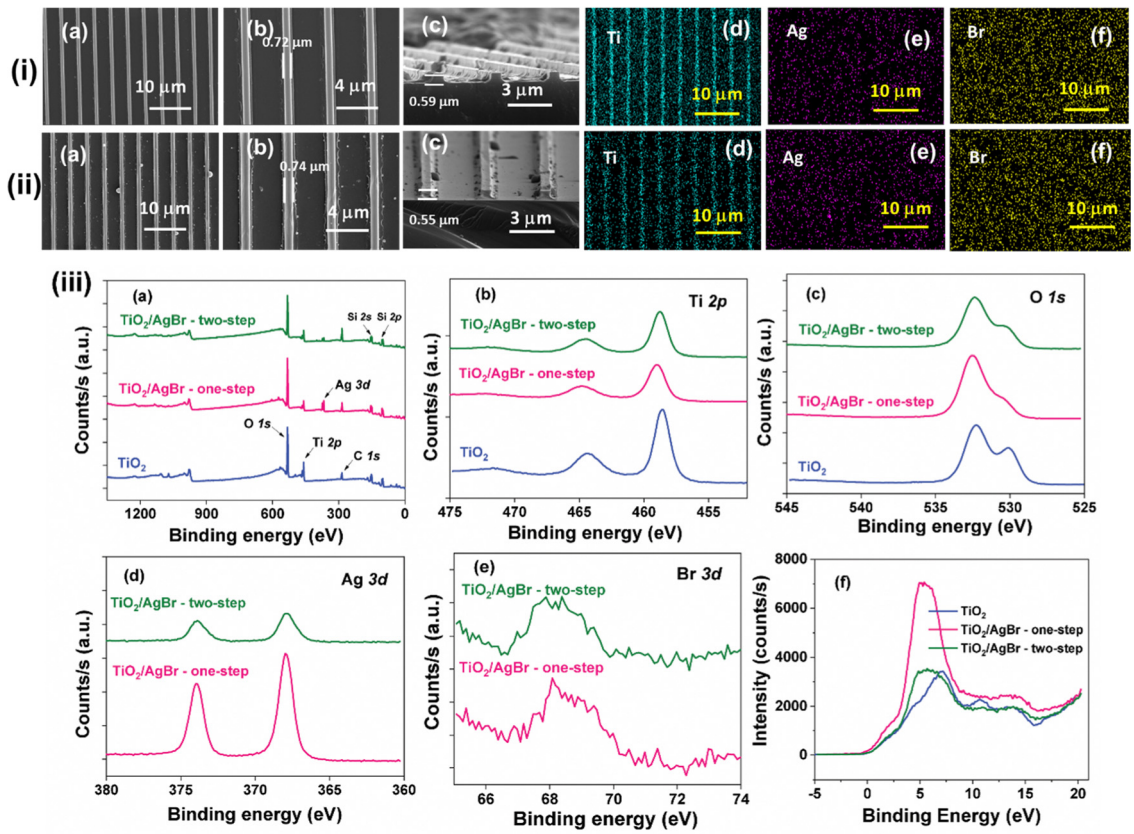

Fig. 6 FE-SEM images (a)–(c) and elemental mapping (d)–(f) of TiO_2/AgBr nanocomposites fabricated through one-step (i) and two-step (ii) methods. (iii) (a) XPS survey scan of TiO_2/AgBr nanocomposites in comparison to pristine TiO_2; XPS narrow scan of (b) Ti 2p, (c) O 1s, (d) Ag 3d and (e) Br 3d of the nanocomposites; (f) overlay of VB spectra of TiO_2 and its nanocomposite with AgBr obtained *via* the two approaches.

visible, likely due to the presence of AgBr nanoparticles. Nevertheless, the elemental mapping analysis revealed the uniform dispersion of silver and bromine across the overall surface. XPS survey scan, narrow scan and VB measurements have been performed over the TiO_2/AgBr nanocomposites and compared to those of pristine TiO_2. The Ti 2p narrow scan analysis in the pristine oxide sample showed the characteristic signals arising from the levels $2p_{3/2}$ and $2p_{1/2}$ at 458.6 eV and 464.3 eV, respectively.[73] Further, the spin–orbit coupling of 5.7 eV, along with a distinctive satellite peak at 471.9 eV, provided confirmation of titanium being present in its '+4' oxidation state in the oxide form. In the one-step nanocomposite, the binding energy of the Ti $2p_{3/2}$ was slightly shifted towards higher energy, measuring 456.0 eV. In the nanocomposite obtained through the two-step method, this binding energy was found at an intermediate value of 458.8 eV. While the spin–orbit coupling value was maintained at 5.7 eV in the nanocomposites, the intensity of the satellite peak was noticeably diminished. In addition, the peak intensity of Ti was found to be relatively lesser in the AgBr deposited samples when compared to the pristine TiO_2. These observations could be attributed to the effective deposition and surface coverage of AgBr over the TiO_2 surface. The surface coverage was further supported by the O 1s narrow scan spectra, which showed a two-humped feature with peak maxima around 530 eV and 532.3 eV, corresponding to lattice oxygen and surface hydroxyl groups of TiO_2, respectively.[73] Additionally, the Ag 3d narrow scan in both the nanocomposites showed a spin–orbit coupling of 6 eV originating from two signature peaks of Ag^+ at 367.5 eV and 373.5 eV, representing the $3d_{5/2}$ and $3d_{3/2}$ levels, respectively.[48] Similarly, a broad peak at ~68 eV, resulting from the overlap between Br $3d_{5/2}$ and $3d_{3/2}$ levels, confirmed the presence of bromide in the nanocomposites.[48] Comparing the two methods, the one-step method exhibited nearly three times higher silver content (2.13 at%) than the two-step method (0.66 at%), indicating superior AgBr loading in the former approach. These observations confirm the successful deposition of AgBr onto the imprinted TiO_2 nanostructures.

To gain insights into the impact of AgBr deposition on TiO_2, XPS VB analyses were conducted on three samples and the findings are depicted in Fig. 6(iii).[73] VB spectra are widely recognized as indicators of occupied electronic states in semiconducting materials. In the case of pristine TiO_2, the VB spectrum exhibited an onset (VB maxima in the band diagram) at ~0.25 eV, with the peak intensity reaching a maximum at the binding energy of 7.2 eV. In contrast, the one-step nanocomposite displayed a VB onset at −0.3 eV, with the peak intensity reaching its maximum at an earlier energy level of ~4.9 eV. Additionally, the overall spectral profile of the one-step nanocomposite was considerably broader than that of pristine TiO_2, suggesting a higher population of electronic states closer to the VB maxima due to the incorporation of AgBr. On the other hand, in the two-step method-derived TiO_2/AgBr nanocomposite, the VB onset resembled that of pristine TiO_2. At the same time, the maximum intensity of the peak was reached at 4.9 eV, similar to the one-step method nanocomposite. Consequently, the VB spectrum of the two-step nanocomposite occupied an intermediate position between the other two samples. These observations highlight the favorable attributes achieved through the one-step method for the photocatalytic process (*vide infra*) and are consistent with the results obtained from XPS narrow scan analyses.

The disinfection performance of TiO_2/AgBr nanocomposites was assessed under dual-mode conditions of dark and light in comparison to AgBr-free TiO_2 (Fig. 7). In the absence of light, the pristine TiO_2 nanostructures showed no bactericidal activity even after 8 h of incubation. In stark contrast, the nanocomposites obtained through both methods demonstrated complete bactericidal activity above 1 h of incubation, which was maintained throughout the 8 h experimental duration. Notably, the one-step method-derived nanocomposite exhibited significantly higher antibacterial activity, likely due to its higher silver content.[48,49,74] It can be noted that the pristine AgBr coating was found to exhibit complete bactericidal activity by 4 h, which was lesser than the nanocomposites. This could be attributed to its poor distribution, as AgBr is known to form discontinuous microflowers.[75] Nevertheless, under light conditions, a significant activity was observed by 2 h, demonstrating the visible-light activity of AgBr. Under visible-light exposure conditions, the photodisinfection performance of the nanocomposites was found to be accelerated, while no effect was observed with pristine TiO_2 nanostructures. The nanocomposites exhibited significant inhibition of bacterial growth within 30 min, while complete inhibition was observed within 60 min. In this case too, the one-step method-derived nanocomposite outperformed the one obtained through the two-step method. To gain additional insights to this observation, we performed a fluorescence-based assay, which revealed a ~3-fold increase in the ROS generation both in one-step and two-step nanocomposites, in comparison to pristine TiO_2 and AgBr. These results additionally corroborate that the higher antibacterial activity of the one-step nanocomposite arises from the higher silver loading (for dark activity) and equivalent amount of ROS generation under light conditions. Deriving insights from XPS, the enhanced disinfection performance of the nanocomposites under light could be attributed to the higher electron density near the VB edge, as observed in the VB spectra (*vide supra*). It is generally known that the exposure of light with an energy equal to or greater than the bandgap of a semiconductor would result in the excitation of an electron in the VB to the conduction band (CB). This process generates a hole in the VB and an electron in the CB. Based on the oxidation/reduction potentials of the VB and CB of the semiconductor, these holes and electrons can react with water, producing reactive oxygen species (ROS) such as hydroxyl and superoxide anion radicals. These radicals can disrupt bacterial membranes, leading to the leakage of intracellular components and eventually leading to the cell death.[52] To investigate the photodisinfection mechanistic pathway, we conducted an experiment using the two-step method-derived nanocomposite by employing isopropanol (IPA) and 4-hydroxy-2,2,6,6-tetramethylpiperidine 1-oxyl (TEMPOL) as the scavengers of hydroxyl and superoxide anion radicals, respectively. The results demonstrated that the

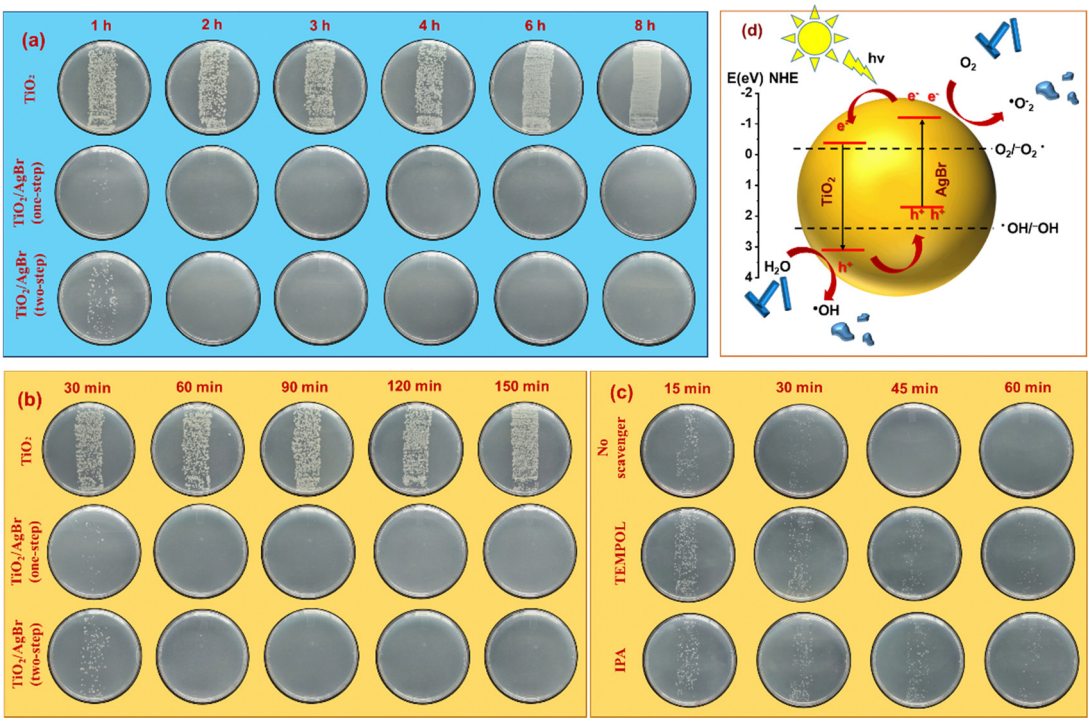

Fig. 7 Antimicrobial efficacy of pristine TiO_2 and TiO_2/AgBr nanocomposites under dark (a) and visible-light (b) conditions. (c) The scavenger effect on the antimicrobial performance of one-step derived TiO_2/AgBr nanocomposite under visible-light conditions. (d) Plausible photodisinfection mechanism, depicting the electron–hole hopping processes leading to ROS generation in the heterojunction of TiO_2/AgBr nanocomposite.

nanocomposite without any radical scavenger exhibited complete photodisinfection performance above 30 min. In contrast, the samples containing IPA and TEMPOL showed decreased photodisinfection efficacy, allowing bacterial growth to persist for up to 1 h. These findings suggest that both types of radicals play a significant role in the photodisinfection process.

3. Conclusions

In summary, we have successfully demonstrated single-source molecular precursor-based CARs in the fabrication of metal oxide nanostructures through direct nanoimprinting. The epoxy- and oxetane-based metal complexes enabled the formulation of imprintable resins, alleviating the requirement of reactive diluents, which in turn allowed to increase the metal content. Consequently, the TGA analyses showed that the net metal oxide content after calcination was higher when the organic content was kept lower. The remarkable adhesion properties of epoxy- and oxetane moieties resulted in excellent film quality when spin-coated. Additionally, their oxygen insensitivity during chemically amplified cross-linking provides an added advantage. The nanoimprinting studies employing representative oxides, like TiO_2, ZrO_2 and Nb_2O_5, showed that their feature size shrinkage was decreased by ~10–30% as opposed to the state-of-the-art olefin-based resins employed in the PSG approach. These results pave the path for future works for further decreasing the feature size shrinkage as well as patterning various other functional inorganic materials.[76–81]

The functionality of the imprinted structures was demonstrated by creating TiO_2/AgBr nanocomposites using one-step and two-step methods and evaluating their antibacterial efficacy under dark-light dual-mode conditions. The nanocomposites exhibited remarkable disinfection performance, surpassing the inactivity of pristine TiO_2 nanostructures. Among the two methods, the one-step method-derived nanocomposite demonstrated superior antibacterial activity, attributed to its higher silver content. In the dark, the one-step method-derived nanocomposites displayed complete bactericidal activity after 1 h of incubation and the antibacterial maintenance was ascertained up to 8 h. In contrast, pristine TiO_2 showed no effect throughout the entire experiment. On the other hand, under visible-light exposure, the nanocomposite exhibited accelerated photodisinfection, inhibiting bacterial growth within 30 min and achieving complete inhibition by 45 min. These findings make the nanocomposites promising as coatings for high-risk areas like hospitals and public places due to their efficient dual-mode disinfection properties. Moreover, this study serves as a foundation for exploring the biological applications of imprinted functional nanomaterials, benefiting the healthcare sector, electronic industry and environmental remediation.

4. Experimental section

4.1. Materials

The reagents titanium(IV) ethoxide, zirconium(IV) *n*-butoxide (80 wt% solution in 1-butanol), niobium(V) ethoxide, glycidol, *tert*-butyl acetoacetate (*t*-BAA), 3-methyl-3-oxetane methanol, toluene, diphenyliodonium hexafluorophosphate (DPHFP), 2′,7′-dichloro-

fluorescein diacetate (DCFH-DA), 4-hydroxy-2,2,6,6-tetramethylpiperidine 1-oxyl (TEMPOL), isopropanol, tetraoctylammonium bromide (TOAB), silver nitrate and 1*H*,1*H*,2*H*,2*H*-perfluorodecyltrichlorosilane were procured from Sigma-Aldrich and used without any further purification unless otherwise mentioned. Sylgard 184 from Sigma-Aldrich was used for fabricating the PDMS molds. The consumables and reagents required for the cell culture experiments, like petriplates, sodium chloride, Luria-Bertani (LB) broth and LB agar were obtained from Himedia Chemicals Pvt. Ltd (India). The Ag–TOAB complex was prepared by reacting silver nitrate and TOAB, as per the literature protocol.

4.2. Synthesis of (oxirane-2-yl)methyl 3-oxobutanoate (glycidyl acetoacetate or epoxy-functionalized acetoacetate (EAA)) and (3-methyloxetane-3-yl)methyl 3-oxobutanoate (oxetane-functionalized acetoacetate (OAA))

EAA was synthesized by following a literature report on *trans*-esterification reaction.[57] Briefly, 0.86 mmol of *t*-BAA was taken in 12 mL of toluene and heated to 85 °C. To this pre-heated ester, a 2 mL toluene solution containing 0.1 mmol of glycidol was slowly added using a syringe. The reaction was stirred under inert atmosphere for 3 hours at 110 °C. After the completion of the reaction, the solvent was evaporated and the product was purified by column chromatography using neutral alumina as the stationary phase and 10% of ethyl acetate in hexane as the mobile phase. The yield of purified EAA was in the range of 40–50%. Following the same protocol, OAA was also synthesized and purified by employing 3-methyl-3-oxetane methanol in place of glycidol. In this case, the yield of purified OAA was found to be significantly higher, to the tune of ~70%.

4.3. Resin formulation

The as-synthesized EAA or OAA was mixed in different ratios with the metal alkoxides and a PAG to formulate the imprintable resins. For instance, the polymerizable TiO_2 resins were prepared by the addition of varying amounts of EAA/OAA to titanium(IV) ethoxide, as mentioned in Table 3. In a typical procedure, $Ti(EAA)_4$ complex has been made by treating one equivalent of $Ti(OEt)_4$ with four equivalents of EAA in a glass vial and subjecting the resultant mixture to magnetic stirring for 10 min under an inert atmosphere. The color of the solution was found to be rapidly turned red, indicating the chelation of EAA with the metal. To this complex, 2 wt% (with respect to EAA) of DPHFP (which is the PAG), was added to formulate the imprintable resin. The above formulation was diluted with equal wt% of toluene to decrease the viscosity during spin-coating and subsequent imprinting. In a similar way, the metal alkoxides were treated with different equivalents of EAA/OAA—as indicated in Table 3—to formulate various compositions of imprintable resins.

Table 3 Proportions of the components used in the different formulations

Sample code	Titanium(IV) ethoxide (mmol)	EAA/OAA (mmol)	PAG (mmol)
$Ti(OEt)_3(EAA)$	1	1	0.0075
$Ti(OEt)_2(EAA)_2$	1	2	0.0150
$Ti(OEt)(EAA)_3$	1	3	0.0225
$Ti(EAA)_4$	1	4	0.0300
$Ti(OEt)_3(OAA)$	1	1	0.0873
$Ti(OEt)_2(OAA)_2$	1	2	0.0174
$Ti(OEt)(OAA)_3$	1	3	0.0262
$Ti(OAA)_4$	1	4	0.0350

4.4. Metal oxide nanoimprinting

Following the standard procedure, PDMS molds were fabricated from a polycarbonate master mold containing ~1.75 and ~2.15 μm line and space, respectively. Also, by treating with 1*H*,1*H*,2*H*,2*H*-per-fluorodecyltrichlorosilane, the surface energy of the mold was decreased to facilitate easy demolding. In a typical nanoimprinting process, the metal-containing resin solution was spin-coated over a silicon wafer (20 mm × 20 mm) at 1200 rpm for 60 s. On top of the spin-coated film, the PDMS mold was gently placed with an application of a slight pressure ensured through a cello tape. The top side of the assembly was then exposed to UV irradiation using a 125 W Hg vapor lamp for 1 min to induce the generation of photoacids in the resin matrix. After the UV exposure, the assembly was subjected to post-exposure baking (PEB) by placing on a hot plate at 110 °C for 3–5 min. After PEB, the PDMS stamp was carefully demolded and the resultant imprints were subjected to calcination at designated temperatures for 1 h to obtain the patterned metal oxides.

4.5. Fabrication of TiO_2/AgBr heterojunctions

Two approaches, namely one-step and two-step, have been adopted to deposit AgBr over the nanoimprinted TiO_2. In the one-step method, the nanoimprint obtained with $Ti(OEt)(OAA)_3$ prior to calcination was spin-coated with a 20 mg mL^{-1} solution of Ag–TOAB in toluene at a rate of 500 rpm for 30 s. This sample was subjected to calcination at 400 °C for 1 h to obtain TiO_2/AgBr-I, where the Roman letter 'I' signifies one-step method. Following a similar procedure, a control AgBr film was also prepared over a bare silicon wafer without TiO_2 nanoimprints on it. In the two-step method, the first step comprises of calcination of $Ti(OEt)(OAA)_3$ nanoimprints to obtain TiO_2 nanostructures, on top of which a 20 mg mL^{-1} solution of Ag–TOAB in toluene was spin-coated as mentioned above. This assembly was calcined at 270 °C for 1 h to obtain TiO_2/AgBr-II.

4.6. Dark-light dual-mode disinfection performance evaluation

Coverslips of ~1.5 cm × 1.5 cm in size containing the nanoimprints of pristine TiO_2, TiO_2/AgBr-I and TiO_2/AgBr-II were chosen for their antibacterial activity under dark and light conditions against *E. coli*. In the experiment under dark conditions, the samples were immersed in a 2 mL solution of 0.9% NaCl, which was added with 20 μL of ~10^6 CFU per mL bacterial culture. At designated time points, the coverslips were intermittently removed from the solution and linearly swiped on the LB agar plate, followed by overnight incubation at 37 °C.

The coverslips were subsequently reintroduced into the bacterial solution and the experiment was continued until reaching the final designated time point. In the light-exposed experiment, the sample submerged in the bacterial culture was subjected to varying time intervals of visible light irradiation (250 W xenon lamp; Scientific Aids & Instruments Corporation (SAIC), India), while all other conditions remained constant.

To derive quantitative information on the ROS generation, DCFH-DA assay was used.[82] For this, a stock solution of 3 mM was prepared in 1 mL of 100% ethanol, from which a secondary stock of 50 μM was prepared in 1× PBS. The substrate were taken in a 24 well plate added with 800 μL of autoclaved millipore water, to which 200 μL of 50 μM DCFH-DA was added to get the final working concentration as 10 μM. The plate was then incubated under light till 1 h, following which the fluorescence was recorded at the excitation wavelength of 488 nm and the emission wavelength of 525 nm.

4.7. Characterization

The synthesized monomers were characterized using Bruker Ascend (400 MHz) NMR spectrophotometer. The chelation and epoxy ring opening polymerization were followed using FT-IR spectrophotometer (JASCO FTIR 4200). The thermal degradation profile and the residual oxide content after pyrolysis of the metal-containing resins were studied through TGA using Shimadzu DTG-60 differential thermal analyzer operated under an air atmosphere. XRD patterns of the TiO_2 thin film samples were recorded using Rigaku Ultima IV X-ray diffractometer (X-ray source: Cu K_α; λ = 1.5418 Å) at a scan rate of 1° min^{-1}. FE-SEM (FEI, Apreo S) was employed to characterize the surface morphological and cross-sectional features of the imprints before and after calcination. XPS measurements were recorded on the nanoimprinted thin films using Thermofisher K-Alpha equipped with an Al K_α X-ray source.

Conflicts of interest

There are no conflicts to declare.

Acknowledgements

The authors would like to thank the Department of Science and Technology (DST) for the financial support (File No.: SPG/2021/004518). Also, the TGA, FT-IR, FE-SEM, XPS and XRD facilities of the Central Analytical Laboratory of BITS Pilani Hyderabad campus are gratefully acknowledged. This work is Dedicated to Prof. Jin-Baek Kim from KAIST for his contributions to lithography.

References

1 A. Kristensen, J. K. Yang, S. I. Bozhevolnyi, S. Link, P. Nordlander, N. J. Halas and N. A. Mortensen, Plasmonic Colour Generation, *Nat. Rev. Mater.*, 2016, **2**, 1–14.
2 M. Saboktakin, X. Ye, S. J. Oh, S. H. Hong, A. T. Fafarman, U. K. Chettiar, N. Engheta, C. B. Murray and C. R. Kagan, Metal-enhanced Upconversion Luminescence Tunable Through Metal Nanoparticle–nanophosphor Separation, *ACS Nano*, 2012, **6**, 8758–8766.
3 X. Qu, J. Li, Z. Yin and H. Zou, New Lithography Technique Based on Electrohydrodynamic Printing Platform, *Org. Electron.*, 2019, **71**, 279–283.
4 G. Liu, S. H. Petrosko, Z. Zheng and C. A. Mirkin, Evolution of Dip-pen Nanolithography (DPN): From Molecular Patterning to Materials Discovery, *Chem. Rev.*, 2020, **120**, 6009–6047.
5 S. Xiong, L. Wan, Y. Ishida, Y. A. Chapuis, G. S. Craig, R. Ruiz and P. F. Nealey, Directed Self-assembly of Triblock Copolymer on Chemical Patterns for Sub-10-nm Nanofabrication *via* Solvent Annealing, *ACS Nano*, 2016, **10**, 7855–7865.
6 A. E. Kandjani, R. Ramanathan, M. Zabara, Y. M. Sabri, S. K. Bhargava and V. Bansal, Long-Range Ordered Crystals of 3D Inorganic–Organic Heterojunctions *via* Colloidal Lithography, *Small Methods*, 2019, **3**, 1900080.
7 M. S. M. Saifullah, N. Tiwale and R. Ganesan, Review of Metal-containing Resists in Electron Beam Lithography: Perspectives for Extreme Ultraviolet Patterning, *J. Micro/Nanopatterning, Mater., Metrol.*, 2022, **21**, 041402.
8 N. Ravi Kiran, M. Chauhan, S. K. Sharma, S. Ghosh and K. E. Gonsalves, Resists for Helium Ion Beam Lithography: Recent Advances, *ACS Appl. Electron. Mater.*, 2020, **2**, 3805–3817.
9 L. Li, X. Liu, S. Pal, S. Wang, C. K. Ober and E. P. Giannelis, Extreme Ultraviolet Resist Materials for Sub-7 nm Patterning, *Chem. Soc. Rev.*, 2017, **46**, 4855–4866.
10 P. Thiyagarajan, H. J. Ahn, J. S. Lee, J. C. Yoon and J. H. Jang, Hierarchical Metal/Semiconductor Nanostructure for Efficient Water Splitting, *Small*, 2013, **9**, 2341–2347.
11 S. Shin, S. A. Woo and J. B. Kim, Diazoketo-functionalized POSS Resists for High Performance Replica Molds of Ultraviolet-nanoimprint Lithography, *Nanotechnology*, 2016, **27**, 475301.
12 R. Ganesan, J. Dumond, M. S. M. Saifullah, S. H. Lim, H. Hussain and H. Y. Low, Direct Patterning of TiO_2 using Step-and-Flash Imprint Lithography, *ACS Nano*, 2012, **6**, 1494–1502.
13 M. Modaresialam, Z. Chehadi, T. Bottein, M. Abbarchi and D. Grosso, Nanoimprint Lithography Processing of Inorganic-based Materials, *Chem. Mater.*, 2021, **33**, 5464–5482.
14 Z. Peng, Y. Zhang, C. L. R. Choi, P. Zhang, T. Wu and Y. K. Chan, Continuous Roller Nanoimprint: Next Generation Lithography, *Nanoscale*, 2023, **15**, 11403–11421.
15 F. Palmieri; M. D. Stewart; J. Wetzel; J. Hao; Y. Nishimura; K. Jen; C. Flannery; B. Li; H.-L. Chao and S. Young, Multilevel Step and Flash Imprint Lithography for Direct Patterning of Dielectrics, *Emerging Lithographic Technologies X*, SPIE, 2006, vol. 6151, pp. 156–164.
16 M. Luo and X. Hu, Direct Imprinting of TiO_2 Patterns on Highly Curved Substrates, *J. Vac. Sci. Technol., B*, 2020, **38**, 062604.

17 S. Lee, S. H. Jung, A. R. Jang, S. I. Yoon, H. S. Shin, H. U. Lee and J. Lee, Large Area Patterning of Residue-free Metal Oxide Nanostructures by Liquid Transfer Imprint Lithography, *Nanotechnology*, 2019, **30**, 235301.

18 J. Ge, B. Ding, S. Hou, M. Luo, D. Nam, H. Duan, H. Gao, Y. C. Lam and H. Li, Rapid Fabrication of Complex Nanostructures Using Room-temperature Ultrasonic Nanoimprinting, *Nat. Commun.*, 2021, **12**, 3146.

19 S. Zhu, Y. Tang, C. Lin, X. Y. Liu and Y. Lin, Recent Advances in Patterning Natural Polymers: from Nanofabrication Techniques to Applications, *Small Methods*, 2021, **5**, 2001060.

20 S. Jo, J. Y. Woo, J. H. Oh, H. C. Shim, S. Seo, E. S. Jeon, M. Kim and C. S. Han, Angle-insensitive Transmission and Reflection of Nanopatterned Dielectric Multilayer Films for Colorful Solar Cells, *ACS Appl. Mater. Interfaces*, 2020, **12**, 29979–29985.

21 K. Kim, B. Ki, K. Choi and J. Oh, Anodic Imprint Lithography: Direct Imprinting of Single Crystalline GaAs with Anodic Stamp, *ACS Nano*, 2019, **13**, 13465–13473.

22 C. Zhang, Y. Song, M. Wang, M. Yin, X. Zhu, L. Tian, H. Wang, X. Chen, Z. Fan and L. Lu, Efficient and Flexible Thin Film Amorphous Silicon Solar Cells on Nanotextured Polymer Substrate Using Sol–gel Based Nanoimprinting Method, *Adv. Funct. Mater.*, 2017, **27**, 1604720.

23 Z. Chehadi, M. Montanari, N. Granchi, M. Modaresialam, M. Koudia, M. Abel, M. Putero, D. Grosso, F. Intonti and M. Abbarchi, Soft Nano-Imprint Lithography of Rare-Earth-Doped Light-Emitting Photonic Metasurface, *Adv. Opt. Mater.*, 2022, **10**, 2201618.

24 J. Zhang, L. Zhang, W. Wang, L. Han, J. C. Jia, Z. W. Tian, Z. Q. Tian and D. Zhan, Contact Electrification Induced Interfacial Reactions and Direct Electrochemical Nanoimprint Lithography in n-type Gallium Arsenate Wafer, *Chem. Sci.*, 2017, **8**, 2407–2412.

25 M. Faustini, C. Boissiere, L. Nicole and D. Grosso, From Chemical Solutions to Inorganic Nanostructured Materials: a Journey into Evaporation-driven Processes, *Chem. Mater.*, 2014, **26**, 709–723.

26 K. Lim, Y. M. Jo, J. W. Yoon and J. H. Lee, Metal Oxide Patterns of One-dimensional Nanofibers: On-demand, Direct-write Fabrication, and Application as a Novel Platform for Gas Detection, *J. Mater. Chem. A*, 2019, **7**, 24919–24928.

27 J. Wang, Z. Ji, X. Xu, T. Chen, B. Chen, G. Gao, J. Ma, X. Nie and X. Xu, Hybrid Lithographic Arbitrary Patterning of TiO_2 Nanorod Arrays, *ACS Omega*, 2022, **7**, 22039–22045.

28 Z. Chehadi, M. Bouabdellaoui, M. Modaresialam, T. Bottein, M. Salvalaglio, M. Bollani, D. Grosso and M. Abbarchi, Scalable Disordered Hyperuniform Architectures *via* Nanoimprint Lithography of Metal Oxides, *ACS Appl. Mater. Interfaces*, 2021, **13**, 37761–37774.

29 T. Bottein, O. Dalstein, M. Putero, A. Cattoni, M. Faustini, M. Abbarchi and D. Grosso, Environment-controlled Sol–gel Soft-NIL Processing for Optimized Titania, Alumina, Silica and Yttria-zirconia Imprinting at Sub-micron Dimensions, *Nanoscale*, 2018, **10**, 1420–1431.

30 S. H. Lim, M. S. M. Saifullah, H. Hussain, W. W. Loh and H. Y. Low, Direct Imprinting of High Resolution TiO_2 Nanostructures, *Nanotechnology*, 2010, **21**, 285303.

31 S. S. Dinachali, M. S. M. Saifullah, R. Ganesan, E. S. Thian and C. He, A Universal Scheme for Patterning of Oxides *via* Thermal Nanoimprint Lithography, *Adv. Funct. Mater.*, 2013, **23**, 2201–2211.

32 R. Kothari, M. Beaulieu, N. Hendricks, S. Li and J. Watkins, Direct Patterning of Robust 1-D, 2-D and 3-D Crystalline Metal Oxide Nanostructures Using Imprint Lithography and Nanoparticle Dispersion Inks, *Chem. Mater.*, 2017, **29**, 3908–3918.

33 R. Ganesan, S. H. Lim, M. S. M. Saifullah, H. Hussain, J. X. Kwok, L. Ryan, H. A. Bo and H. Y. Low, Direct Nanoimprinting of Metal Oxides by in situ Thermal Co-polymerization of their Methacrylates, *J. Mater. Chem.*, 2011, **21**, 4484–4492.

34 R. Ganesan, S. S. Dinachali, S. H. Lim, M. S. M. Saifullah, W. T. Chong, A. H. Lim, J. J. Yong, E. San Thian, C. He and H. Y. Low, Direct Nanoimprint Lithography of Al_2O_3 Using a Chelated Monomer-based Precursor, *Nanotechnology*, 2012, **23**, 315304.

35 S. S. Dinachali, J. Dumond, M. S. M. Saifullah, K. K. Ansah-Antwi, R. Ganesan, E. S. Thian and C. He, Large Area, Facile Oxide Nanofabrication *via* Step-and-Flash Imprint Lithography of Metal–Organic Hybrid Resins, *ACS Appl. Mater. Interfaces*, 2013, **5**, 13113–13123.

36 R. Nagarjuna, M. S. M. Saifullah and R. Ganesan, Oxygen Insensitive Thiol–ene Photo-click Chemistry for Direct Imprint Lithography of Oxides, *RSC Adv.*, 2018, **8**, 11403–11411.

37 T. H. Oh; R. Ganesan; J. M. Yoon and J. B. Kim, Negative Nanomolecular Resists based on Calix [4] Resorcinarene, *Advances in Resist Technology and Processing XXIII*, SPIE, 2006, vol. 6153, pp. 788–797.

38 S. K. Sehmi, C. Lourenco, K. Alkhuder, S. D. Pike, S. Noimark, C. K. Williams, M. S. Shaffer, I. P. Parkin, A. J. MacRobert and E. Allan, Antibacterial Surfaces with Activity Against Antimicrobial Resistant Bacterial Pathogens and Endospores, *ACS Infect. Dis.*, 2020, **6**, 939–946.

39 C. Hobson, A. N. Chan and G. D. Wright, The Antibiotic Resistome: a Guide for the Discovery of Natural Products as Antimicrobial Agents, *Chem. Rev.*, 2021, **121**, 3464–3494.

40 C. Murray, K. Ikuta, F. Sharara, L. Swetschinski, G. R. Aguilar, A. Gray and M. Naghavi, Global Burden of Bacterial Antimicrobial Resistance in 2019: a Systematic Analysis, *Lancet*, 2022, **399**, 629–655.

41 X. L. Hu, Y. Shang, K. C. Yan, A. C. Sedgwick, H. Q. Gan, G. R. Chen, X. P. He, T. D. James and D. Chen, Low-dimensional Nanomaterials for Antibacterial Applications, *J. Mater. Chem. B*, 2021, **9**, 3640–3661.

42 M. Nazeri, H. Sedaghat, R. Rafiei, M. A. Farzin and S. M. H. Mashkani, Er_2TiO_5@Ag Nanocomposites: Enhanced Photocatalysis and Bacteria Inactivation, and Cytotoxicity, *J. Rare Earths*, 2023, DOI: 10.1016/j.jre.2023.10.017.

43 K. Wang, S. Zhan, D. Zhang, H. Sun, X. Jin and J. Wang, In situ Grown Monolayer N–Doped Graphene and ZnO on

$ZnFe_2O_4$ Hollow Spheres for Efficient Photocatalytic Tetracycline Degradation, *Colloids Surf., A*, 2021, **618**, 126362.

44 F. Dundar Arisoy, K. W. Kolewe, B. Homyak, I. S. Kurtz, J. D. Schiffman and J. J. Watkins, Bioinspired Photocatalytic Shark-skin Surfaces with Antibacterial and Antifouling Activity *via* Nanoimprint Lithography, *ACS Appl. Mater. Interfaces*, 2018, **10**, 20055–20063.

45 H. Mude, P. A. Maroju, A. Balapure, R. Ganesan and J. Ray Dutta, Quaternized Polydopamine Coatings for Anchoring Molecularly Dispersed Broad-spectrum Antimicrobial Silver Salts, *ACS Appl. Bio Mater.*, 2021, **4**, 8396–8406.

46 P. A. Maroju, P. Tata, A. Balapure, J. R. Dutta and R. Ganesan, *Lactobacillus Amylovorus* Derived Lipase-mediated Silver Derivatization Over Poly(ε-caprolactone) Towards Antimicrobial Coatings, *Enzyme Microb. Technol.*, 2021, **150**, 109888.

47 W. Huang, S. Ruan, M. Zhao, R. Xu, Z. Chen, G. Zhihong and H. Song, Visible-light-driven Photocatalytic Inactivation of *Escherichia coli* by 0D/2D CeO_2/g-C_3N_4 Heterojunction: Bactericidal Performance and Mechanism, *J. Environ. Chem. Eng.*, 2021, **9**, 106759.

48 A. Balapure, Y. Nikhariya, N. S. Sriteja Boppudi, R. Ganesan and J. Ray Dutta, Highly Dispersed Nanocomposite of AgBr in g-C_3N_4 Matrix Exhibiting Efficient Antibacterial Effect on Drought-resistant Pseudomonas Putida Under Dark and Light Conditions, *ACS Appl. Mater. Interfaces*, 2020, **12**, 21481–21493.

49 C. Chen, D. Wang, Y. Li, H. Huang and Y. Ke, Flower-like AgBr/CeO_2 Z-scheme Heterojunction Photocatalyst with Enhanced Visible Light Photocatalytic and Antibacterial Activities, *Appl. Surf. Sci.*, 2021, **565**, 150534.

50 H. Zhang, X. Zhang, M. Zhu, H. Li, Y. Zhao, X. Han, L. Jin and H. Shan, Antibacterial Performance of a Gold-Loaded g-C_3N_4 Nanocomposite System in Visible Light-Dark Dual Mode, *ChemPlusChem*, 2020, **85**, 2722–2730.

51 A. Balapure, H. Mude, P. Tata, J. R. Dutta and R. Ganesan, Sublimable Xanthate-mediated Solid-State Synthesis of Highly Interspersed g-C_3N_4/Ag_2S Nanocomposites Exhibiting Efficient Bactericidal Effects Both Under Dark and Light Conditions, *J. Environ. Chem. Eng.*, 2021, **9**, 106065.

52 M. M. Francis, A. Thakur, A. Balapure, J. R. Dutta and R. Ganesan, Fabricating Effective Heterojunction in Metal-organic Framework-derived Self-cleanable and Dark/visible-light Dual Mode Antimicrobial CuO/AgX (X= Cl, Br, or I) Nanocomposites, *Chem. Eng. J.*, 2022, **446**, 137363.

53 L. Doveri, A. Taglietti, P. Grisoli, P. Pallavicini and G. Dacarro, Dual Mode Antibacterial Surfaces Based on Prussian Blue and Silver Nanoparticles, *Dalton Trans.*, 2023, **52**, 452–460.

54 J. Wang, P. Li, N. Wang, J. Wang and D. Xing, Antibacterial Features of Material Surface: Strong Enough to Serve as Antibiotics?, *J. Mater. Chem. B*, 2023, **11**, 280–302.

55 F. H. Haghighi, M. Mercurio, S. Cerra, T. A. Salamone, R. Bianymotlagh, C. Palocci, V. R. Spica and I. Fratoddi, Surface Modification of TiO_2 Nanoparticles with Organic Molecules and their Biological Applications, *J. Mater. Chem. B*, 2023, **11**, 2334–2366.

56 J. Du, R. Liu, E. Zhu, H. Guo, Z. Li, C. Liu and G. Che, Visible-light-induced Bactericidal Properties of a Novel Thiophene-based Linear Conjugated Polymer/TiO_2 Heterojunction, *J. Mater. Chem. B*, 2022, **10**, 737–747.

57 W. Nottingham and J. Witzemann, Transacetoacetylation with *tert*-butyl Acetoacetate: Synthetic Application, *J. Org. Chem.*, 1991, **56**, 1713–1718.

58 A. Legaustic, F. Babonneau and J. Livage, Structural Investigation of the Hydrolysis-Condensation Process of Titanium Alkoxides $Ti(OR)_4$ (OR= OPri, OEt) Modified by Acetylacetone. 1. Study of the Alkoxide Modification, *Chem. Mater.*, 1989, **1**, 240–247.

59 G. Nikolic, S. Zlatkovic, M. Cakic, S. Cakic, C. Lacnjevac and Z. Rajic, Fast Fourier Transform IR Characterization of Epoxy GY Systems Crosslinked with Aliphatic and Cycloaliphatic EH Polyamine Adducts, *Sensors*, 2010, **10**, 684–696.

60 Y. M. Evtushenko, V. Ivanov and B. Zaitsev, Determination of Epoxide and Hydroxyl Groups in Epoxide Resins by IR Spectrometry, *J. Anal. Chem.*, 2003, **58**, 347–350.

61 F. Zhan, X. E. Cheng and W. Shi, Cationic UV Curing Behavior and Thermal Properties of Oxetane-Modified Polysiloxane Prepared from Tetraethyl Orthosilicate, *J. Appl. Polym. Sci.*, 2012, **123**, 717–724.

62 R. Nagarjuna, S. Roy and R. Ganesan, Polymerizable Sol–gel Precursor Mediated Synthesis of TiO_2 Supported Zeolite-4A and its Photodegradation of Methylene Blue, *Microporous Mesoporous Mater.*, 2015, **211**, 1–8.

63 S. Challagulla, R. Nagarjuna, R. Ganesan and S. Roy, Acrylate-based Polymerizable Sol–gel Synthesis of Magnetically Recoverable TiO_2 Supported Fe_3O_4 for Cr(VI) Photoreduction in Aerobic Atmosphere, *ACS Sustainable Chem. Eng.*, 2016, **4**, 974–982.

64 L. Song, A. Abdelsamie, C. J. Schaffer, V. Korstgens, W. Wang, T. Wang, E. D. Indari, T. Froschl, N. Husing and T. Haeberle, A Low Temperature Route Toward Hierarchically Structured Titania Films for Thin Hybrid Solar Cells, *Adv. Funct. Mater.*, 2016, **26**, 7084–7093.

65 B. Jalvo, M. Faraldos, A. Bahamonde and R. Rosal, Antibacterial Surfaces Prepared by Electrospray Coating of Photocatalytic Nanoparticles, *Chem. Eng. J.*, 2018, **334**, 1108–1118.

66 S. Challagulla, K. Tarafder, R. Ganesan and S. Roy, All that Glitters is Not Gold: a Probe into Photocatalytic Nitrate Reduction Mechanism Over Noble Metal Doped and Undoped TiO_2, *J. Phys. Chem. C*, 2017, **121**, 27406–27416.

67 Y. Gong, Y. Wu, Y. Xu, L. Li, C. Li, X. Liu and L. Niu, All-solid-state Z-scheme CdTe/TiO_2 Heterostructure Photocatalysts with Enhanced Visible-light Photocatalytic Degradation of Antibiotic Waste Water, *Chem. Eng. J.*, 2018, **350**, 257–267.

68 J. Li, Z. Jin, Y. Zhang, D. Liu, A. Ma, Y. Sun, X. Li, Q. Cai and J. Gui, Ag-induced Anatase-rutile TiO_{2-x} Heterojunction Facilitating the Photogenerated Carrier Separation in Visible-light Irradiation, *J. Alloys Compd.*, 2022, **909**, 164815.

69 K. Wang, S. Zhan, H. Sun, D. Zhang and J. Wang, Hollow Porous Core–Shell $ZnFe_2O_4$/AgCl Nanocubes Coated with

EDTA and Ag Nanoparticles for Enhanced Photocatalytic Performances of Visible–Light–Driven, *Chem. Eng. J.*, 2020, **400**, 125908.

70 X. Li, T. Wan, J. Qiu, H. Wei, F. Qin, Y. Wang, Y. Liao, Z. Huang and X. Tan, In-situ Photocalorimetry-fluorescence Spectroscopy Studies of RhB Photocatalysis Over Z-scheme g-C_3N_4@Ag@Ag_3PO_4 Nanocomposites: a Pseudo-Zero-Order Rather than a First-order Process, *Appl. Catal., B*, 2017, **217**, 591–602.

71 P. A. Maroju, R. Ganesan and J. Ray Dutta, Probing the Effects of Antimicrobial-Lysozyme Derivatization on Enzymatic Degradation of Poly(ε-caprolactone) Film and Fiber, *Macromol. Biosci.*, 2023, 2300296.

72 S. Feizpoor and A. Habibi-Yangjeh, Integration of Ag_2WO_4 and AgBr with TiO_2 to Fabricate Ternary Nanocomposites: Novel Plasmonic Photocatalysts with Remarkable Activity Under Visible Light, *Mater. Res. Bull.*, 2018, **99**, 93–102.

73 A. Balapure and R. Ganesan, Anatase versus Triphasic TiO_2: Near-identical Synthesis and Comparative Structure-sensitive Photocatalytic Degradation of Methylene Blue and 4-chlorophenol, *J. Colloid Interface Sci.*, 2021, **581**, 205–217.

74 H. Mude, P. Tata, T. Jamma, R. Ganesan and J. Ray Dutta, Fabrication and Facile Surface Derivatization of Poly(ε-caprolactone)-Based Wound Dressing Materials Imparting Anti-Infective, Excessive Biofluid Drainage, and Easy-to-Peel Characteristics, *Adv. Ther.*, 2023, **6**, 2300015.

75 S. Pawar, B. R. Teja, R. Nagarjuna, R. Ganesan and A. Nag, Probing the Surface Composition Effect of Silver-Gold Alloy in SERS Efficiency, *Colloids Surf., A*, 2019, **578**, 123638.

76 M. Gayrard, J. Voronkoff, C. Boissiere, D. Montero, L. Rozes, A. Cattoni, J. Peron and M. Faustini, Replacing Metals with Oxides in Metal-assisted Chemical Etching Enables Direct Fabrication of Silicon Nanowires by Solution Processing, *Nano Lett.*, 2021, **21**, 2310–2317.

77 M. C. Sharps, R. T. Frederick, M. L. Javitz, G. S. Herman, D. W. Johnson and J. E. Hutchison, Organotin Carboxylate Reagents for Nanopatterning: Chemical Transformations During Direct-write Electron Beam Processes, *Chem. Mater.*, 2019, **31**, 4840–4850.

78 D. W. Lee, D. H. Kim, J. Y. Oh and D. S. Seo, A Fine-ordered Nanostructured Bismuth Tin Oxide Thin Film Constructed *via* Sol–gel Nanopatterning for Liquid Crystal System, *Appl. Phys. A: Mater. Sci. Process.*, 2022, **128**, 1–12.

79 Y. Wang, J. A. Pan, H. Wu and D. V. Talapin, Direct Wavelength-selective Optical and Electron-beam Lithography of Functional Inorganic Nanomaterials, *ACS Nano*, 2019, **13**, 13917–13931.

80 C. C. Yeh, H. W. Zan and O. Soppera, Solution-Based Micro- and Nanoscale Metal Oxide Structures Formed by Direct Patterning for Electro-Optical Applications, *Adv. Mater.*, 2018, **30**, 1800923.

81 Y. Wang, I. Fedin, H. Zhang and D. V. Talapin, Direct Optical Lithography of Functional Inorganic Nanomaterials, *Science*, 2017, **357**, 385–388.

82 C. Hwang, M. H. Choi, H. E. Kim, S. H. Jeong and J. U. Park, Reactive Oxygen Species-Generating Hydrogel Platform for Enhanced Antibacterial Therapy, *NPG Asia Mater.*, 2022, **14**, 72.